AIAA JOURNAL
Vol. 49, No. 3, March 2011

Formulation of Analytical Design Derivatives for Nonlinear Unsteady Aeroelasticity

Bret Stanford* and Philip Beran†
U.S. Air Force Research Laboratory, Wright–Patterson Air Force Base, Ohio 45433

DOI: 10.2514/1.J050713

The engineering community has devoted considerable recent attention to nontraditional aircraft concepts, where nonlinear, unsteady, coupled aeroelastic physics have been found to drive the design process. There is a lack of current research aimed at bringing these physical concepts into a formal optimization environment, which is the focus of the current work. A numerical framework is developed to capture the unsteady aeroelastic interactions between a nonlinear shell and the surrounding flow. An analytical sensitivity analysis of the model is then discussed, computing the derivative of the aerodynamic force production with respect to a large vector of structural design variables. The work concludes with a series of gradient-based aeroelastic optimization studies, demonstrating the efficacy of analytical gradients towards tailoring the complex interaction between fluid and structure for optimal performance.

Nomenclature

$\boldsymbol{C}$	=	damping matrix
$\boldsymbol{C}_1$, $\boldsymbol{C}_2$	=	wing-wing and wake-wing influence matrices
$\boldsymbol{C}_{w1}$, $\boldsymbol{C}_{w2}$	=	wing-wing and wake-wing streamwise influence matrices
C_{Do}	=	constant viscous drag coefficient, $C_{Do} = -C_{To}$
C_L	=	lift coefficient, $F_Z/q_\infty/S$
C_P	=	power coefficient, $P/q_\infty/U_\infty/S$
C_T	=	thrust coefficient, $-F_X/q_\infty/S$
c, b	=	wing chord and span, m
E	=	elastic modulus, GPa
$\boldsymbol{F}$, $\boldsymbol{F}_{\text{sa}}$	=	external force and sensitivity analysis force vectors
F_X, F_Z	=	aerodynamic forces, n
$\boldsymbol{g}$, $\boldsymbol{G}$	=	objective functions or constraints
h_a	=	plunge amplitude, m
$\boldsymbol{I_o}$, $\boldsymbol{I_f}$	=	time step integration bounds
i	=	time step
$\boldsymbol{K}$, $\boldsymbol{K}_{\text{ext}}$, $\boldsymbol{K}_{\text{sa}}$	=	tangent stiffness, external stiffness, and sensitivity analysis stiffness matrices
k	=	reduced frequency, $\omega \cdot c/2/U_\infty$
$\boldsymbol{L}$	=	velocity along the outward normal of each collocation point
$\boldsymbol{M}$	=	mass matrix
N_{DV}	=	number of design variables
$\boldsymbol{P}$	=	internal force vector
P	=	required power input, w
$\boldsymbol{p}$	=	aerodynamic pressures
$\boldsymbol{Q}$	=	interpolation matrix
q_∞	=	dynamic pressure, $0.5 \cdot \rho_{\text{fluid}} \cdot U_\infty^2$
Re	=	Reynolds number, $\rho_{\text{fluid}} \cdot U_\infty \cdot c/\mu$
S	=	wing area, m^2
St	=	Strouhal number, $k \cdot h_a/c$
T	=	time period, s
$\boldsymbol{t_o}$, $\boldsymbol{t_f}$	=	time-integration bounds
t	=	time, s
t_{wing}	=	plate thickness, mm
U_∞	=	external flow velocity, m/s
$\boldsymbol{u}$	=	shell deformation solution vector
$\boldsymbol{w}$	=	induced velocity at each collocation point
$\boldsymbol{X_r}$	=	rigid body motion vector
XYZ	=	fixed inertial coordinate system
$\boldsymbol{x}$	=	design variables
x_{min}, x_{max}	=	side constraints
xyz	=	body-attached moving coordinate system
$\boldsymbol{z}$	=	vector with the x, y, and z coordinates of each node along the wing
$\boldsymbol{z_o}$	=	undeformed wing shape
α	=	angle of attack, deg.
Γ, $\Gamma_{\boldsymbol{w}}$	=	wing and wake circulation (strength)
η	=	efficiency, C_T/C_P
μ	=	dynamic viscosity, $\text{N} \cdot \text{s/m}^2$
ν	=	Poisson's ratio
ρ_{fluid}, ρ_{wing}	=	fluid and plate density, kg/m^3
ω	=	frequency, rad/s

I. Introduction

FEW options exist for optimization with a large number of design variables other than gradient-based methods. Many techniques for computing these design derivatives exist, though again constrained by the large number of design variables under consideration, only analytical methods are typically feasible. These methods can use either direct or adjoint techniques. The former directly computes the derivative of the system response with respect to the design variables, while the latter skips this (typically) superfluous quantity in favor of an adjoint vector, which is independent of the design variables. The use of an adjoint method is generally considered more cost effective when the number of design variables is greater than the number of constraints [1].

The use of moderate-fidelity computational tools for the design and optimization of aeroelastic structures is well-founded in the literature. The lower computational cost allows for rapid exploration of the highly-complex and multidimensional design space. Bias errors between the moderate-fidelity tool and the true system may exist, but if the tool is able to capture (to some extent) the physics that drive the aeroelastic design, the analytical derivatives will be highly useful [2]. Of course, care must still be taken to tie the model to known results from either experiments or higher-fidelity numerical models. Furthermore, moderate-fidelity tools are an attractive option

Presented as Paper 2010-2999 at the 51st AIAA/ASME/ASCE/AHS/ASC Structures, Structural Dynamics, and Materials Conference, Orlando, FL, 12–15 April 2010; received 25 June 2010; revision received 10 September 2010; accepted for publication 28 October 2010.

*National Research Council Postdoctoral Researcher; bret.stanford@wpafb.af.mil.

†Principal Research Aerospace Engineer; philip.beran@wpafb.af.mil. Associate Fellow AIAA.

in the sense that analytical design sensitivities can be practically computed for a large number of design variables without resorting to an adjoint method, which is notoriously cumbersome for nonlinear unsteady physics [3]. The differential equation for the adjoint vector is provided with terminal conditions, and must be integrated in reverse [4]: the system response and the adjoint cannot be computed simultaneously, and the storage costs can be large [5].

For moderate-fidelity tools, the Jacobian can usually be factorized and stored with little effort, and the direct method requires the solution of a single system of equations at each time step with multiple right-hand-sides (the number of design variables). The cost of such an endeavor will grow linearly with the number of design variables, but the multiple right-hand-sides of the linear system can be computed simultaneously, and the cost of proportionality should be small (for cases given next, each additional design variable adds a cost of 0.1% of the effort required to solve for a single right-hand-side). Conversely, for some high-fidelity tools the Jacobian is never explicitly factorized (Navier–Stokes solvers, for example): the cost of multiple right-hand-sides will grow quickly with the number of design variables, and adjoint methods are required [6].

Examples of fully-coupled aeroelastic sensitivities (computed analytically, either with the adjoint or the direct method) are not common in the literature; derivatives of unsteady systems are rarer still. Some recent examples of the former category are given by Stanford and Ifju [7] (3-D linear wing structure coupled to a steady vortex lattice method), Giunta [8], Maute et al. [9] and Martins et al. [6] (3-D linear wing structure coupled to a steady Euler solver), and Barcelos and Maute [10] (3-D linear wing structure coupled to a steady Navier–Stokes solver). For unsteady systems, Seyranian [11] and Odaka and Furuya [12] linearize the aeroelastic equations of motion in order to differentiate the relevant eigenvalue problem governing flutter instabilities (using linear wing structures coupled to aerodynamic strip theory and supersonic piston theory, respectively). Finally, recent work by Mani and Mavriplis [13] examine unsteady aeroelastic adjoint gradients with time-marching methods, by coupling a two-dimensional pitch-and-plunge airfoil to an unsteady Euler solver. The resulting algorithm is used to optimize the shape of an airfoil for flutter prevention.

There is a lack of current research pertaining to three-dimensional nonlinear unsteady aeroelastic sensitivities. Such gradients should be extremely useful for the design and optimization of a varied suite of aeroelastic systems, and are the focus of this work. The aeroelastic solver used here couples an unsteady vortex lattice method to a nonlinear shell dynamics solver for implicit time marching with a fluid–structure subiteration convergence loop. The structural solver (corotational approximation of the updated Lagrangian approach) can be considered a high-fidelity tool, capable of computing very large rotations, displacements, and strains. The aerodynamic solver, however, though truly three-dimensional and unsteady, is an inviscid technique: at each time step, the strength of a lattice of vortex rings along the wing is computed by specifying the wing to be a stream-surface of the flow (no penetration). A continuously evolving wake is approximated by shedding a row of rings from the trailing edge at each step.

The goal of this work is to develop a framework for the computation of the analytical design derivatives of the preceding unsteady aeroelastic solver with a direct method. Specifically, it is desired to compute the derivative of time-averaged aerodynamic force quantities (lift, thrust, efficiency, etc.) with respect to a large vector of structural design variables in an analytical manner. The remainder of this work is organized as follows: first, both the aeroelastic framework and the concomitant sensitivity analysis are formulated in detail. The solver is then used to compute the aeroelastic response of a chosen test case for comparison with known experimental results. The derivative of the time-averaged aerodynamic forces are computed with respect to the thickness of each triangular finite element, and verified with a costly finite difference study. The work concludes with a series of disparate gradient-based aeroelastic optimization studies, demonstrating the efficacy of analytical gradients towards tailoring the complex interaction between fluid and structure for optimal performance.

II. Aeroelastic Modeling

An illustration of the problem definition considered here can be found in Fig. 1. There exists a fixed inertial coordinate system (XYZ) as well as a moving coordinate system (xyz) attached to the root of a flexible rectangular wing. The undeformed shape of the wing is drawn as a flat plate, though the methods described next are valid for any initial shape. Similarly, no control surfaces are considered over the wing, but the following aeroelastic formulation does not prohibit their eventual inclusion. Rigid body motions are incorporated in the time-dependent vector $\boldsymbol{X}_r$ as well as three Euler angles which transform the inertial system to the body-attached system. An external flow travels with a velocity U_∞ along the X-axis, aeroelastic behavior is assumed to be symmetric across the XZ plane (i.e., a pair wing exists across this plane), and the wing is clamped along the entire body-attached x-axis.

The structural model used in this work is a nonlinear shell model computed via a corotational approximation of the updated Lagrangian approach [14]. The wing structure is discretized into triangular finite elements, with 6 degrees of freedom (three displacements and three rotations) per node. The equations of motion at time step i are

$$\boldsymbol{M} \cdot \ddot{\boldsymbol{u}}^i + \boldsymbol{C} \cdot \dot{\boldsymbol{u}}^i + \boldsymbol{P}^i = \boldsymbol{F}^i \tag{1}$$

where $\boldsymbol{u}^i$ is the solution vector measured in the body-attached coordinate system, along with this first two time derivatives. The consistent mass matrix $\boldsymbol{M}$ and the structural damping matrix $\boldsymbol{C}$ (indicative of the energy dissipated by the vibrating structure) are constant entities, and have no time step superscript. $\boldsymbol{F}^i$ is a vector of external forces composed of both inertial (due to the rigid body motion) and aerodynamic forces. $\boldsymbol{P}^i$ is a vector of internal forces, a nonlinear function of the shell deformation. The tangent stiffness matrix is computed analytically as

$$\boldsymbol{K}^i = \frac{\partial \boldsymbol{P}^i}{\partial \boldsymbol{u}^i} \tag{2}$$

The stiffness matrix contains in-plane membrane terms (modeled with a linear-strain triangle element with drilling degrees of freedom, LST), out-of-plane bending terms (modeled with a discrete Kirchhoff triangle element, DKT), nonlinear stress stiffening, and spin-softening terms (representing a coupling between elastic deformation and rigid body rotations of the body-attached coordinate system, if any) [15]. Equation (1) is integrated with a generalized-α method [16], using the tangent stiffness matrix (as well as the external stiffness matrix described next) to drive the residual below a specified tolerance at each time step via the Newton–Rapshon method. Time derivatives are approximated with standard Newmark terms. Further information concerning the nonlinear shell dynamics model, as well as verification studies, can be found in [17].

Having solved Eq. (1), the shape of the wing, again measured in the body-attached coordinate system, is updated:

$$\boldsymbol{z}^i = \boldsymbol{z}_o + \boldsymbol{Q} \cdot \boldsymbol{u}^i \tag{3}$$

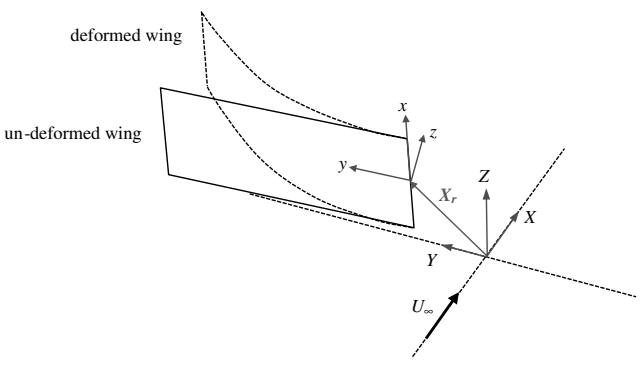

Fig. 1 Flexible wing illustration and coordinate system definition.

$\boldsymbol{z}^i$ is a vector which contains the x, y, and z coordinates of each node along the wing, $\boldsymbol{z}_o$ is the shape of the undeformed wing (Fig. 1), and $\boldsymbol{Q}$ is an interpolation matrix. The deformation vector $\boldsymbol{u}^i$ contains displacements and rotations of each free finite element node: $\boldsymbol{Q}$ removes the rotations and adds back in the displacements of the fixed (i.e., clamped) nodes, which are zero.

The unsteady vortex lattice solver proceeds as follows [18]: the shape of the wing at time step i is first defined by Eq. (3). This geometry is then transformed into the inertial coordinate system, where the wing is discretized into a lattice of vortex ring singularities, with a collocation point located at the center of each. The vortex rings along the trailing edge of the wing are convected into the wake, while the strength (circulation) of each of these rings is set equal to that computed at the previous time step, and held fixed. A system of equations is developed and solved for the new circulation distribution throughout the wing: velocities due to wing-wing interactions, wake-wing interactions, freestream velocities, wing rotations/translations, and wing deformation must all cancel each other in the direction normal to each collocation point. This stipulates that the wing becomes a stream-surface of the flow:

$$\boldsymbol{C}_1^i \cdot \Gamma^i + \boldsymbol{C}_2^i \cdot \Gamma_w^i = \boldsymbol{L}^i \tag{4}$$

where $\boldsymbol{C}_1^i$ and $\boldsymbol{C}_2^i$ are wing-wing and wake-wing influence matrices (as computed with the Biot–Savart law). The source vector $\boldsymbol{L}^i$ is the velocity along the outward normal of each collocation point due to the wing movement, Γ_w^i is the strength of the wake, and Γ^i is the unknown strength of the wing, which is computed by inverting the wing-wing influence matrix. The local streamline at each wake ring can be computed through the wing-wake and wake-wake interactions, and subsequently deformed [19]. It should also be noted that the influence matrices operate under the assumption of symmetry about the XZ plane (Fig. 1); a pair wing is assumed to exist across this plane.

The wing circulation distribution can be used to compute the induced velocity at each collocation point (for induced drag computations):

$$\boldsymbol{w}^i = \boldsymbol{C}_{w1}^i \cdot \Gamma^i + \boldsymbol{C}_{w2}^i \cdot \Gamma_w^i \tag{5}$$

These influence matrices are similar to those found in Eq. (4), but only include the streamwise portions of each vortex ring [18]. The velocity for these terms is not resolved along the outward normal of each panel, but along the local lift vector of each panel (perpendicular to the flow). The pressures $\boldsymbol{p}^i$ and integrated forces (lift, thrust, etc.) can be subsequently computed as well.

Aeroelastic coupling is performed with an implicit time marching scheme via a fluid–structure subiteration loop within each time step, as seen in Fig. 2. Within an aeroelastic subiteration, the wing grid is meshed via Eq. (3), where it should be emphasized that the vortex rings follow the wing as it deforms, and are therefore not parallel to the freestream velocity vector. The geometry information is used to compute the pressure distribution $\boldsymbol{p}^i$ over the wing via the unsteady vortex lattice method, which in turn is used to compute work-equivalent nodal forces normal to the deflected wing surface [15]. These forces, along with known values of the structural deformation, velocity, acceleration, external forces, and internal forces from the previous $i-1$ time step, are used within a Newton–Raphson update loop to compute the deformation at the current step i [Eq. (1)]. The iterations commence within the updated Lagrangian loop until the residual is driven below a specified tolerance. The aeroelastic subiterations commence until an aeroelastic residual (defined here as the norm of the difference in the pressure vector computed at consecutive subiterations) is driven below a specified tolerance. Having converged, the vortex lattice method can be used to find the new shape of the wake, and the time step counter is increased to $i+1$.

III. Aeroelastic Sensitivity Analysis

For this work, it is assumed that an optimization framework will contain objective functions and constraints formulated as time-averaged quantities:

$$g = \int_o^{t_f} G \cdot \mathrm{d}t \sim \sum_{i=I_o}^{I_f} \omega^i \cdot G^i \tag{6}$$

where G^i is a scalar property of the aeroelastic deformation at time step i. It is desired to numerically integrate over a certain time period of interest (assumed to lie between time steps I_o and I_f), where ω^i are weighting coefficients (reflecting a trapezoidal time-integration scheme). If the objective functions or constraints contain quantities at a single time step (a peak load condition, for example), then I_o and I_f will be identical. For this work, G^i is an aerodynamic force-based quantity, generically written as

$$G^i = f(\boldsymbol{z}^i, \boldsymbol{z}^{i-1}, \boldsymbol{w}^i, \Gamma^i, \Gamma^{i-1}) \tag{7}$$

All time derivatives (wing velocities for the source vector $\boldsymbol{L}^i$, as well as $\mathrm{d}\Gamma^i/\mathrm{d}t$ terms for the unsteady Bernoulli equation [18]) are computed with a backwards finite difference equation, so information is needed at the previous time step to compute forces within the current time step.

The design variables are given by $\boldsymbol{x}$, which for this work will be a large vector containing structural parameters. Specifically, the thickness of each finite element is used, but any structural sizing variable could be used in the formulation given next. For gradient-based optimization, the derivative of the scalar objective/constraint with respect to $\boldsymbol{x}$ is needed:

$$\frac{\mathrm{d}g}{\mathrm{d}\boldsymbol{x}} = \sum_{i=I_o}^{I_f} \omega^i \cdot \frac{\mathrm{d}G^i}{\mathrm{d}\boldsymbol{x}} \tag{8}$$

This derivative can be computed with the chain rule, via the five dependencies listed in Eq. (7):

$$\frac{\mathrm{d}G^i}{\mathrm{d}\boldsymbol{x}} = \frac{\partial G^i}{\partial \boldsymbol{z}^i} \cdot \boldsymbol{Q} \cdot \frac{\mathrm{d}\boldsymbol{u}^i}{\mathrm{d}\boldsymbol{x}} + \frac{\partial G^i}{\partial \boldsymbol{z}^{i-1}} \cdot \boldsymbol{Q} \cdot \frac{\mathrm{d}\boldsymbol{u}^{i-1}}{\mathrm{d}\boldsymbol{x}} + \frac{\partial G^i}{\partial \boldsymbol{w}^i} \cdot \frac{\mathrm{d}\boldsymbol{w}^i}{\mathrm{d}\boldsymbol{x}} + \frac{\partial G^i}{\partial \Gamma^i} \cdot \frac{\mathrm{d}\Gamma^i}{\mathrm{d}\boldsymbol{x}} + \frac{\partial G^i}{\partial \Gamma^{i-1}} \cdot \frac{\mathrm{d}\Gamma^{i-1}}{\mathrm{d}\boldsymbol{x}} \tag{9}$$

The first terms in the five products in Eq. (9) can be computed directly, as G^i is a known function of these vectors; the remaining terms (essentially the derivative of the aeroelastic system response) require additional effort. The interpolation matrix $\boldsymbol{Q}$ [essentially $\partial \boldsymbol{z}^i/\partial \boldsymbol{u}^i$ via Eq. (3)] is constant in time and independent of the design variables: because the vortex rings follow the structure as it deforms, the process by which information is transferred from the structural solver to the aerodynamic solver is assumed not to vary.

From the structural model, the following dependencies are observed:

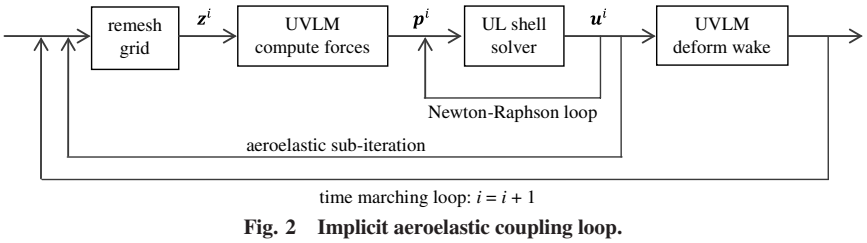

Fig. 2 Implicit aeroelastic coupling loop.

$$\boldsymbol{M} = f(\boldsymbol{x}) \qquad \boldsymbol{C} = f(\boldsymbol{x}) \qquad \boldsymbol{P}^i = f(\boldsymbol{x}, \boldsymbol{u}^i) \qquad \boldsymbol{F}^i = f(\boldsymbol{x}, \boldsymbol{u}^i, \boldsymbol{p}^i) \tag{10}$$

The mass and damping matrices are only functions of $\boldsymbol{x}$, while the internal force vector depends (nonlinearly) upon the solution vector $\boldsymbol{u}^i$ as well [Eq. (2)]. The external force vector depends upon $\boldsymbol{x}$ (in the case of large rigid body motions, heavier wing structures have stronger inertial forces), the pressure $\boldsymbol{p}^i$, and the deformation $\boldsymbol{u}^i$. The pressure loads are typically nonconservative follower forces: wing deformation changes the direction of the loads, hence the last dependency. The derivative of the finite element analysis [Eq. (1)] is

$$\frac{\mathrm{d}\boldsymbol{M}}{\mathrm{d}\boldsymbol{x}} \cdot \ddot{\boldsymbol{u}}^i + \boldsymbol{M} \cdot \frac{\mathrm{d}\ddot{\boldsymbol{u}}^i}{\mathrm{d}\boldsymbol{x}} + \frac{\mathrm{d}\boldsymbol{C}}{\mathrm{d}\boldsymbol{x}} \cdot \dot{\boldsymbol{u}}^i + \boldsymbol{C} \cdot \frac{\mathrm{d}\dot{\boldsymbol{u}}^i}{\mathrm{d}\boldsymbol{x}} + \boldsymbol{K}^i \cdot \frac{\mathrm{d}\boldsymbol{u}^i}{\mathrm{d}\boldsymbol{x}} + \frac{\partial \boldsymbol{P}^i}{\partial \boldsymbol{x}} = \frac{\mathrm{d}\boldsymbol{F}^i}{\mathrm{d}\boldsymbol{x}} \tag{11}$$

where the derivatives of the mass and damping matrices are known triply-indexed terms [17]. The derivative of the force vector can be expanded based upon the three dependencies of Eq. (10):

$$\frac{\mathrm{d}\boldsymbol{F}^i}{\mathrm{d}\boldsymbol{x}} = \frac{\partial \boldsymbol{F}^i}{\partial \boldsymbol{x}} + \frac{\partial \boldsymbol{F}^i}{\partial \boldsymbol{p}^i} \cdot \frac{\mathrm{d}\boldsymbol{p}^i}{\mathrm{d}\boldsymbol{x}} + \frac{\partial \boldsymbol{F}^i}{\partial \boldsymbol{u}^i} \cdot \frac{\mathrm{d}\boldsymbol{u}^i}{\mathrm{d}\boldsymbol{x}} \tag{12}$$

The first term is an explicit dependence upon $\boldsymbol{x}$ (typically via the inertial forces), whereas the latter two products are implicit dependencies through the pressure and structural deformation. The dependence of the force on the pressure is easily computed, while the dependence upon the deformation (due to the nonconservative pressure loads) is the skew-symmetric external stiffness matrix [15]:

$$\frac{\partial \boldsymbol{F}^i}{\partial \boldsymbol{u}^i} = \boldsymbol{K}^i_{\text{ext}} \tag{13}$$

Similar to Eq. (7), the aerodynamic pressures depend upon the wing geometry and circulation at the current and previous time step (due to the finite differences used for the unsteady Bernoulli equation):

$$\boldsymbol{p}^i = f(\boldsymbol{z}^i, \boldsymbol{z}^{i-1}, \Gamma^i, \Gamma^{i-1}) \tag{14}$$

As preceding, the derivative can be expanded through the chain rule:

$$\frac{\mathrm{d}\boldsymbol{p}^i}{\mathrm{d}\boldsymbol{x}} = \frac{\partial \boldsymbol{p}^i}{\partial \boldsymbol{z}^i} \cdot \boldsymbol{Q} \cdot \frac{\mathrm{d}\boldsymbol{u}^i}{\mathrm{d}\boldsymbol{x}} + \frac{\partial \boldsymbol{p}^i}{\partial \boldsymbol{z}^{i-1}} \cdot \boldsymbol{Q} \cdot \frac{\mathrm{d}\boldsymbol{u}^{i-1}}{\mathrm{d}\boldsymbol{x}} + \frac{\partial \boldsymbol{p}^i}{\partial \Gamma^i} \cdot \frac{\mathrm{d}\Gamma^i}{\mathrm{d}\boldsymbol{x}} + \frac{\partial \boldsymbol{p}^i}{\partial \Gamma^{i-1}} \cdot \frac{\mathrm{d}\Gamma^{i-1}}{\mathrm{d}\boldsymbol{x}} \tag{15}$$

The derivative of the wing circulation with respect to $\boldsymbol{x}$ requires a differentiation of the unsteady vortex lattice method. The following dependencies are observed:

$$\boldsymbol{C}^i_1 = f(\boldsymbol{z}^i) \qquad \boldsymbol{C}^i_2 = f(\boldsymbol{z}^i, \boldsymbol{z}^{i-1}, \ldots, \boldsymbol{z}^1) \qquad \boldsymbol{L}^i = f(\boldsymbol{z}^i, \boldsymbol{z}^{i-1}) \tag{16}$$

The wing-wing influence matrix is only a function of the wing geometry at the current time step (as computed with the Biot–Savart law). The wake-wing influence matrix is a function of the current wing geometry and the current wake geometry. The wake geometry, however, is a function of the previous wake and wing geometry: a recursive relationship exists back to the initial time step. The end result is that $\boldsymbol{C}^i_2$ is a function of the wing geometry at every preceding time step. The source vector $\boldsymbol{L}^i$ contains wing velocity terms, which are computed with finite differences. As such, the geometry at both the current and the previous time steps are required. Similar dependencies can be written for the influence matrices of Eq. (5):

$$\boldsymbol{C}^i_{w1} = f(\boldsymbol{z}^i, \boldsymbol{z}^{i-1}) \qquad \boldsymbol{C}^i_{w2} = f(\boldsymbol{z}^i, \boldsymbol{z}^{i-1}, \ldots, \boldsymbol{z}^1) \tag{17}$$

As can be inferred from Eqs. (4) and (16), the wing circulation Γ^i is an explicit function of the wing geometry at every time step between one and i, while the wake circulation Γ^i_w depends upon geometry up to time step $i-1$:

$$\Gamma^i = f(\boldsymbol{z}^i, \boldsymbol{z}^{i-1}, \ldots, \boldsymbol{z}^1) \qquad \Gamma^i_w = f(\boldsymbol{z}^{i-1}, \boldsymbol{z}^{i-2}, \ldots, \boldsymbol{z}^1) \tag{18}$$

The circulation derivatives needed in Eq. (15) can thus be computed with a chain rule, summing terms from the initial step to the current step i:

$$\frac{\mathrm{d}\Gamma^i}{\mathrm{d}\boldsymbol{x}} = \sum_{j=1}^{i} \left(\frac{\partial \Gamma^i}{\partial \boldsymbol{z}^j} \cdot \boldsymbol{Q} \cdot \frac{\mathrm{d}\boldsymbol{u}^j}{\mathrm{d}\boldsymbol{x}} \right) \tag{19}$$

The sensitivities $\partial\Gamma^i/\partial \boldsymbol{z}^j$ are computed by differentiating the no-penetration condition [Eq. (4)]:

$$\boldsymbol{C}^i_1 \cdot \frac{\partial \Gamma^i}{\partial \boldsymbol{z}^j} = \begin{cases} \frac{\partial \boldsymbol{L}^i}{\partial \boldsymbol{z}^i} - \frac{\partial \boldsymbol{C}^i_1}{\partial \boldsymbol{z}^i} \cdot \Gamma^i - \frac{\partial \boldsymbol{C}^i_2}{\partial \boldsymbol{z}^i} \cdot \Gamma^i_w, & j = i \\ \frac{\partial \boldsymbol{L}^i}{\partial \boldsymbol{z}^{i-1}} - \frac{\partial \boldsymbol{C}^i_2}{\partial \boldsymbol{z}^{i-1}} \cdot \Gamma^i_w - \boldsymbol{C}^i_2 \cdot \frac{\partial \Gamma^i_w}{\partial \boldsymbol{z}^{i-1}}, & j = i-1 \\ -\frac{\partial \boldsymbol{C}^i_2}{\partial \boldsymbol{z}^j} \cdot \Gamma^i_w - \boldsymbol{C}^i_2 \cdot \frac{\partial \Gamma^i_w}{\partial \boldsymbol{z}^j}, & j < i-1 \end{cases} \tag{20}$$

A piecewise expression is required because $\boldsymbol{L}^i$ is only a function of $\boldsymbol{z}^i$ and $\boldsymbol{z}^{i-1}$ [Eq. (16)], and the wake circulation at step i is not a function of the geometry at step i. Derivatives of the influence matrices are triply-indexed terms, computed by differentiating the Biot–Savart law. Derivatives of the wake terms (as well as the sensitivity of $\boldsymbol{C}^i_2$ upon the geometry at previous time steps) require differentiating the wake shedding and updating algorithms, as these terms provide the only connection between the forces generated at disparate time steps. Further information can be found in [19].

Each of the piecewise expressions requires the solution to a system of equations with multiple right-hand-sides (equal to the size of $\boldsymbol{z}^i$, or 3 times the number of nodes), a hallmark of the direct method of analytical differentiation of discrete systems. As the influence matrix will not be particularly large, the computational cost of such an endeavor will grow slowly with the mesh density. Equation (19) can then be inserted into Eq. (15), and like-terms grouped together [which involves removing the last two terms from the summation of Eq. (19)]:

$$\frac{\mathrm{d}\boldsymbol{p}^i}{\mathrm{d}\boldsymbol{x}} = \left(\frac{\partial \boldsymbol{p}^i}{\partial \Gamma^i} \cdot \frac{\partial \Gamma^i}{\partial \boldsymbol{z}^i} + \frac{\partial \boldsymbol{p}^i}{\partial \boldsymbol{z}^i} \right) \cdot \boldsymbol{Q} \cdot \frac{\mathrm{d}\boldsymbol{u}^i}{\mathrm{d}\boldsymbol{x}} + \left(\frac{\partial \boldsymbol{p}^i}{\partial \Gamma^i} \cdot \frac{\partial \Gamma^i}{\partial \boldsymbol{z}^{i-1}} + \frac{\partial \boldsymbol{p}^i}{\partial \boldsymbol{z}^{i-1}} \right) \cdot \boldsymbol{Q} \cdot \frac{\mathrm{d}\boldsymbol{u}^{i-1}}{\mathrm{d}\boldsymbol{x}} + \frac{\partial \boldsymbol{p}^i}{\partial \Gamma^i} \cdot \sum_{j=1}^{i-2} \left(\frac{\partial \Gamma^i}{\partial \boldsymbol{z}^j} \cdot \boldsymbol{Q} \cdot \frac{\mathrm{d}\boldsymbol{u}^j}{\mathrm{d}\boldsymbol{x}} \right) + \frac{\partial \boldsymbol{p}^i}{\partial \Gamma^{i-1}} \cdot \frac{\mathrm{d}\Gamma^{i-1}}{\mathrm{d}\boldsymbol{x}} \tag{21}$$

Equation (21) can then be inserted into Eq. (12), which in turn can be inserted into Eq. (11). Terms containing $\mathrm{d}\boldsymbol{u}^i/\mathrm{d}\boldsymbol{x}$, as well as its time derivatives are brought to the right side of Eq. (11), while the remainder of the terms are brought to the left side. Equation (11) can then be rewritten as

$$\boldsymbol{M} \cdot \frac{\mathrm{d}\ddot{\boldsymbol{u}}^i}{\mathrm{d}\boldsymbol{x}} + \boldsymbol{C} \cdot \frac{\mathrm{d}\dot{\boldsymbol{u}}^i}{\mathrm{d}\boldsymbol{x}} + \left(\boldsymbol{K}^i - \boldsymbol{K}^i_{\text{ext}} - \frac{\partial \boldsymbol{F}^i}{\partial \boldsymbol{p}^i} \cdot \left(\frac{\partial \boldsymbol{p}^i}{\partial \Gamma^i} \cdot \frac{\partial \Gamma^i}{\partial \boldsymbol{z}^i} + \frac{\partial \boldsymbol{p}^i}{\partial \boldsymbol{z}^i} \right) \cdot \boldsymbol{Q} \right) \cdot \frac{\mathrm{d}\boldsymbol{u}^i}{\mathrm{d}\boldsymbol{x}} = \frac{\partial \boldsymbol{F}^i}{\partial \boldsymbol{x}} - \frac{\mathrm{d}\boldsymbol{M}}{\mathrm{d}\boldsymbol{x}} \cdot \ddot{\boldsymbol{u}}^i - \frac{\mathrm{d}\boldsymbol{C}}{\mathrm{d}\boldsymbol{x}} \cdot \dot{\boldsymbol{u}}^i - \frac{\partial \boldsymbol{P}^i}{\partial \boldsymbol{x}} + \frac{\partial \boldsymbol{F}^i}{\partial \boldsymbol{p}^i} \cdot \left(\frac{\partial \boldsymbol{p}^i}{\partial \Gamma^i} \cdot \frac{\partial \Gamma^i}{\partial \boldsymbol{z}^{i-1}} + \frac{\partial \boldsymbol{p}^i}{\partial \boldsymbol{z}^{i-1}} \right) \cdot \boldsymbol{Q} \cdot \frac{\mathrm{d}\boldsymbol{u}^{i-1}}{\mathrm{d}\boldsymbol{x}} + \frac{\partial \boldsymbol{F}^i}{\partial \boldsymbol{p}^i} \cdot \frac{\partial \boldsymbol{p}^i}{\partial \Gamma^i} \cdot \sum_{j=1}^{i-2} \left(\frac{\partial \Gamma^i}{\partial \boldsymbol{z}^j} \cdot \boldsymbol{Q} \cdot \frac{\mathrm{d}\boldsymbol{u}^j}{\mathrm{d}\boldsymbol{x}} \right) + \frac{\partial \boldsymbol{F}^i}{\partial \boldsymbol{p}^i} \cdot \frac{\partial \boldsymbol{p}^i}{\partial \Gamma^{i-1}} \cdot \frac{\mathrm{d}\Gamma^{i-1}}{\mathrm{d}\boldsymbol{x}} \tag{22}$$

Equation (22) represents a second equation that must be solved at each time step in conjunction with Eq. (1), to compute $\mathrm{d}\boldsymbol{u}^i/\mathrm{d}\boldsymbol{x}$ as it evolves with time. At time step i, every term on the right side of Eq. (22) is known: $\mathrm{d}\boldsymbol{u}^j/\mathrm{d}\boldsymbol{x}$ is known from the previous j time steps, as is $\mathrm{d}\Gamma^{i-1}/\mathrm{d}\boldsymbol{x}$ [Eq. (19)]. Furthermore, the time derivatives of $\boldsymbol{u}^i$ will also be known, as Eq. (1) must be solved at the time step i step before Eq. (22) can be. Equation (22) can be written compactly as

$$\boldsymbol{M} \cdot \frac{\mathrm{d}\ddot{\boldsymbol{u}}^i}{\mathrm{d}\boldsymbol{x}} + \boldsymbol{C} \cdot \frac{\mathrm{d}\dot{\boldsymbol{u}}^i}{\mathrm{d}\boldsymbol{x}} + \boldsymbol{K}^i_{\text{sa}} \cdot \frac{\mathrm{d}\boldsymbol{u}^i}{\mathrm{d}\boldsymbol{x}} = \boldsymbol{F}^i_{\text{sa}} \tag{23}$$

Equation (23) is a linear set of differential equations with time-dependent coefficients ($\boldsymbol{K}^i_{\text{sa}}$ is defined a priori at each time step, and

does not depend upon $\mathrm{d}\boldsymbol{u}^i/\mathrm{d}\boldsymbol{x}$) and multiple right-hand-sides, due, as before, to the use of the direct method of differentiation. $\boldsymbol{F}^i_{\mathrm{sa}}$ and $\mathrm{d}\boldsymbol{u}^i/\mathrm{d}\boldsymbol{x}$ (as well as the latter's time derivatives) are matrices of size $N_{\mathrm{DOF}} \times N_{\mathrm{DV}}$, where the former is the number of free degrees of freedom in the finite element method, and the latter is the number of design variables (length of $\boldsymbol{x}$). As with the system response, Eq. (23) is integrated with a generalized-α method, using Newmark terms to approximate the time derivatives.

The derivative of the induced velocity is also needed in Eq. (9). As with the circulation, the downwash at time step i is an explicit function of the wing geometry at every previous time step:

$$\frac{\mathrm{d}\boldsymbol{w}^i}{\mathrm{d}\boldsymbol{x}} = \sum_{j=1}^{i}\left(\frac{\partial \boldsymbol{w}^i}{\partial \boldsymbol{z}^j}\cdot \boldsymbol{Q}\cdot\frac{\mathrm{d}\boldsymbol{u}^j}{\mathrm{d}\boldsymbol{x}}\right) \tag{24}$$

The derivative of the induced velocity with the respect to the wing shape is computed in a similar manner to Eq. (20), with a piecewise expression:

$$\frac{\partial \boldsymbol{w}^i}{\partial \boldsymbol{z}^j} = \begin{cases} \frac{\partial \boldsymbol{C}^i_{w1}}{\partial z^i}\cdot\Gamma^i + \boldsymbol{C}^i_{w1}\cdot\frac{\partial \Gamma^i}{\partial z^i} + \frac{\partial \boldsymbol{C}^i_{w2}}{\partial z^i}\cdot\Gamma^i_w, & j=i \\ \frac{\partial \boldsymbol{C}^i_{w1}}{\partial z^{i-1}}\cdot\Gamma^i + \boldsymbol{C}^i_{w1}\cdot\frac{\partial \Gamma^i}{\partial z^{i-1}} + \frac{\partial \boldsymbol{C}^i_{w2}}{\partial z^{i-1}}\cdot\Gamma^i_w + \boldsymbol{C}^i_{w2}\cdot\frac{\partial \Gamma^i_w}{\partial z^{i-1}}, & j=i-1 \\ \boldsymbol{C}^i_{w1}\cdot\frac{\partial \Gamma^i}{\partial z^j} + \frac{\partial \boldsymbol{C}^i_{w2}}{\partial z^j}\cdot\Gamma^i_w + \boldsymbol{C}^i_{w2}\cdot\frac{\partial \Gamma^i_w}{\partial z^j}, & j<i-1 \end{cases} \tag{25}$$

Having solved Eq. (23) at a given time step, the relevant terms can be inserted into Eq. (24), and everything needed to evaluate $\mathrm{d}G^i/\mathrm{d}\boldsymbol{x}$ in Eq. (9) is then available. Integration of both the system response [Eq. (1)] and the sensitivity analysis [Eq. (23)] proceeds through time step I_f, at which point $\mathrm{d}g/\mathrm{d}\boldsymbol{x}$ of Eq. (8) can be evaluated.

IV. Model Validation

The unsteady aeroelastic framework detailed preceding is validated against experimental results found in the work of Heathcote et al. [20]. Specifically, a steel rectangular wing undergoes a pure oscillatory plunge motion in a water tunnel, thus generating a propulsive thrust force. Various system parameters are given in Table 1. For this study, the steel sheet is a uniform thickness of 1 mm, which is covered with a flexible rubber cast into a NACA0012 mold. As the rubber is not thought to add to the stiffness of the wing, and the vortex lattice method does not incorporate wing thickness, the mold is ignored for the computational framework. As noted preceding, flow is symmetric about the root chord and the wing is clamped (in the body-attached system) along the entire root. Plunging motion is a cosine profile along the Z-axis only:

$$\boldsymbol{X}_r = \{\,0 \quad 0 \quad h_a\cdot\cos(\omega\cdot t)\,\} \tag{26}$$

The resulting Reynolds number (30,000), reduced frequency (1.821) and Strouhal number (0.318) all fall within the expected range of flapping micro air vehicle wings. Such a system is expected to leverage unsteady, nonlinear, three-dimensional aeroelasticity for optimal performance [17], and is thus a suitable case study for the analysis and sensitivity framework described preceding.

The same wing mesh is used for both the structural shell model and the unsteady vortex lattice method. The latter discretizes the wing into quadrilateral rings, each of which is divided into two triangular shell elements for the structural solver. The wing is discretized into 30 semispan panels and 10 chordwise panels, providing 300 vortex rings for the aerodynamic solver and 600 triangular elements for the structural solver (for this test case, as well as the cases given next). Unless stated otherwise, each plunging cycle is divided into 50 time steps, and 2 cycles are found to be sufficient for the aeroelastic response to set up into a periodic state.

Table 1 Aeroelastic parameters for plunging wing case

Property	Value	Property	Value
Chord, c	0.1 m	Elastic modulus, E	210 GPa
Semispan, $b/2$	0.3 m	Poisson's ratio, ν	0.3
Flow velocity, U_∞	3 m/s	Plate density, ρ_{wing}	7800 kg/m^3
Flow density, ρ_{fluid}	1000 kg/m^3	Plate thickness, t_{wing}	1 mm
Plunge amplitude, h_a	0.0175 m	Plunge frequency, ω	10.92 rad/s

For both the aeroelastic subiteration loop and the updated Lagrangian loop shown in Fig. 2, the specified tolerance on the norm of the residual vectors is 10^{-6}. The Newton–Raphson loop typically converges in less than 10 iterations, though the aeroelastic loop may require between 20 and 40 iterations, and underrelaxation (with a parameter of 0.7) is required to prevent the solution from diverging. This is because the level of coupling for cases run in water is very high:, i.e., the aerodynamic forces are large and substantially effected by the nature of the shell deformation. Further cases discussed next are run in air, where the aeroelastic loop converges much faster (less than 10 iterations), and underrelaxation is not required.

Heathcote et al. [20] report that the elastic wing deformation during the plunging cycle is dominated by the first bending mode (though the geometric nonlinearity provides spanwise foreshortening of the wing as well), with a roughly-sinusoidal trend in time. Similar results are found with the current computational model: normalized root and tip histories are given in Fig. 3. Experimental data is provided some time after the plunging motion has initiated, though the current numerical data is only simulated over two plunging cycles, with the motion initiated at $t=0$. Initial displacement and velocity ($\boldsymbol{u}^0$ and $\dot{\boldsymbol{u}}^0$) are both specified as zero, and as such, the initial tip position computed with the aeroelastic model coincides with the normalized root position ($Z/h_a = 1$). The initial transients of the aeroelastic response decay quickly in time (as the plunging motion is in water); the measured and computed tip position compare very well after the first quarter-cycle, with a peak error of $0.142\cdot h_a$. The aerodynamic forces over the wing provide an amplification of the tip motion with a moderate phase lag behind the root motion.

Time histories of the thrust coefficient are given in Fig. 4, for both rigid and flexible wings. A constant viscous drag coefficient (C_{Do}) of 0.028 is added to all computed thrust coefficients, as measured from the experiment at a reduced frequency of zero. The characteristic frequency of the thrust coefficient is twice that seen in Fig. 3, as positive thrust will be generated during both the up and the downstroke. This is due to a well-known phenomenon, wherein the positive lift vector generated during the downstroke is tilted forward in order to remain perpendicular to the flow vector that results from the combined plunging/forward motion. Similarly, the negative lift

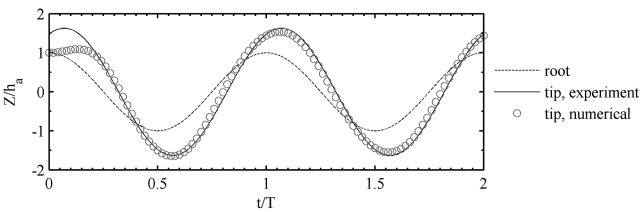

Fig. 3 Normalized tip and root positions of the plunging wing, as compared with experimental data [20].

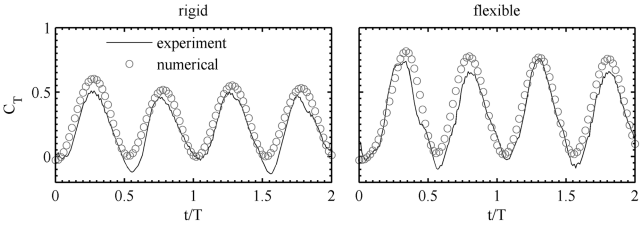

Fig. 4 Thrust produced by rigid (left) and flexible (right) wings, as compared with experimental data [20].

vector is tilted forward during the upstroke. The advent of wing flexibility increases the thrust, due to the fact that the bending deformation increases the tip velocity through the downstroke (as seen in Fig. 3), increasing the angle of attack of each flexible wing section, and thus the forces.

The aeroelastic framework described in this work is able to predict the increase in thrust due to flexibility, but all thrust values are moderately overpredicted as compared with the experimental data. The experiment indicates an increase in the peak thrust coefficient from 0.501 to 0.752, while the model computes an increase from 0.551 to 0.767. This overprediction is certainly due to an inability to predict drag forces due to viscous effects (shear forces, flow separation, etc.). The experimental data predicts higher drag at the bottom of the stroke than the top, which is presumably an artifact of the experimental setup (water tunnel), as there should be little difference between the two positions. Regardless, the effect of wing flexibility upon the aeroelastic response is correctly demonstrated which is encouraging from a sensitivity analysis and optimization standpoint. The correct prediction of the change in system response due to a finite change in a structural variable matters far more than accurate prediction of the value of the response metric itself.

V. Gradient Verification

As noted preceding, for this work the set of design variables $\boldsymbol{x}$ is the thickness of each triangular finite element. The baseline value used preceding, and for the results given in this section, is a uniform thickness of 1 mm. Six hundred finite elements are used in the discretization, and so there are an equal number of design variables. Three time-dependent aerodynamic force-based scalar functions [G^i, Eq. (7)] are of interest: the lift coefficient, thrust coefficient, and power coefficient, where the evolution of the thrust is explicitly given in Fig. 4. Four time-averaged objective functions [g, Eq. (6)] are used: the preceding three, as well as the propulsive efficiency η (the ratio of the time-averaged thrust and power coefficients), computed between $t/T = 2$ and 3. As preceding, each plunging cycle is divided into 50 time steps. All results are taken with the system parameters listed in Table 1.

Sensitivity analysis results are given in Figs. 5 and 6: the derivative of the time-dependent scalar functions with respect to the thickness of 2 disparate finite elements ($\mathrm{d}G^i/\mathrm{d}\boldsymbol{x}$ at the leading edge of the root, and at the trailing edge of the tip). The results computed from the analytical framework detailed preceding are compared with numerical finite differences, where the step size is $\Delta\boldsymbol{x} = 10^{-5}$ mm (found via trial and error, though steps of 10^{-4} mm and 10^{-6} mm were not found to change the first three decimal places of the gradients). The comparison is very good, with percentage-difference errors generally less than 0.1%. It should be emphasized here that the finite differences require the baseline system response, plus one additional simulation for the design variable of interest. The analytical sensitivity analysis, however, requires a single run for both the system response and the gradient with respect to all of the design variables at once, albeit with a larger computational cost [the development and solution of Eq. (23)]. As noted preceding, each additional design variable adds a cost of 0.1% of the effort required to solve for a single right-hand-side; the cost of proportionality for multiple right-hand-sides in Eq. (23) is very low. For this case, the sensitivity analysis framework required 10 times more simulation time than a standard system response run (where a single system response took approximately 1 h on a 3.2-GHz Intel Xeon processor with 16 GB RAM); analytical design derivatives become worthwhile when the number of design variables is greater than ten.

Like the system response seen in Figs. 3 and 4, the time history of the derivatives $\mathrm{d}G^i/\mathrm{d}\boldsymbol{x}$ seen in Figs. 5 and 6 similarly set up into a

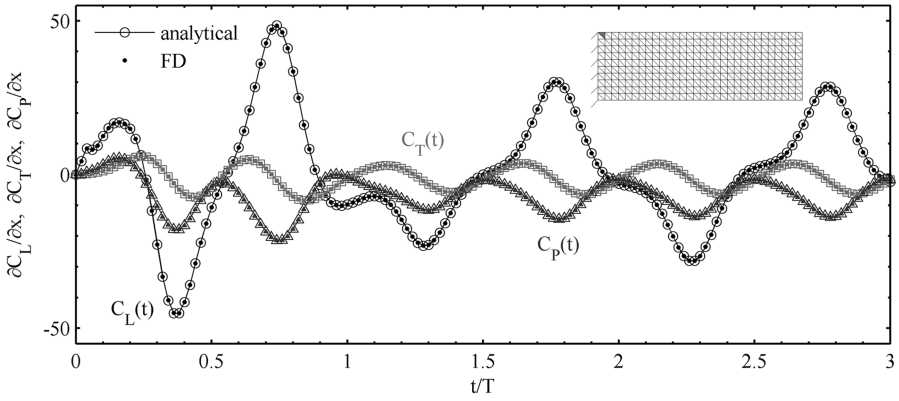

Fig. 5 The derivative of the time-dependent C_L, C_T, and C_P with respect to the thickness of an element at the leading edge of the root. Results are given for analytical sensitivities and numerical finite differences.

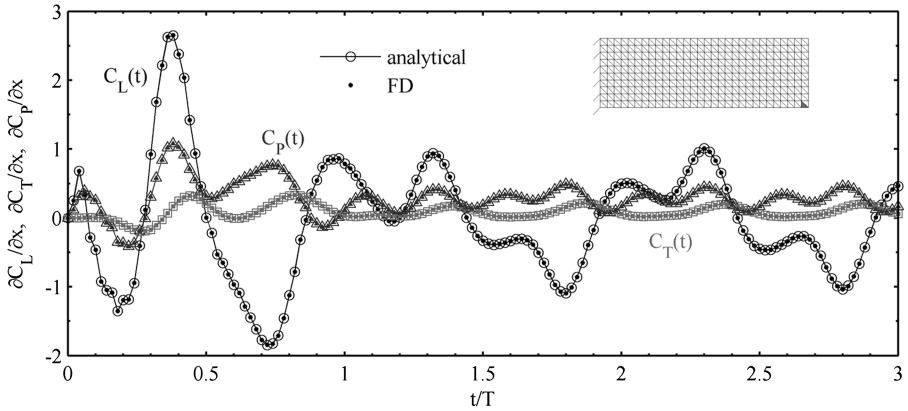

Fig. 6 The derivative of the time-dependent C_L, C_T, and C_P with respect to the thickness of an element at the trailing edge of the tip. Results are given for analytical sensitivities and numerical finite differences.

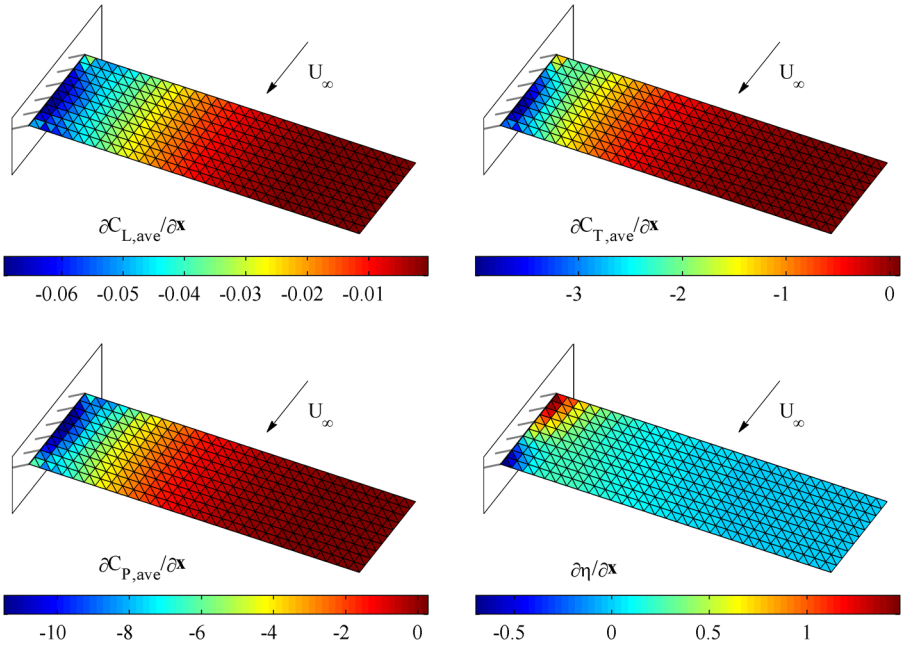

Fig. 7 The derivative of the cycle-averaged lift, thrust, power, and propulsive efficiency with respect to the thickness of each finite element.

time-periodic response. The harmonic content is generally higher, however, and the cyclic behavior takes longer to develop (roughly three plunging cycles, whereas the system response takes only two). The derivative of the lift coefficient is generally larger than the power or thrust gradients, though the mean of its cyclic response is zero. As such, the cycle-averaged lift gradients will be zero, whereas thrust and power gradients will not. This is as expected; the plunging motion is symmetric [Eq. (26)] and the lift generated during both strokes should be equal and opposite, independent of aeroelastic behavior (and hence, structural composition).

The derivatives of the cycle-averaged scalar functions (as well as the propulsive efficiency) are given in Fig. 7 with respect to the thickness of each finite element in the structural mesh, found by integrating under the curves given in Figs. 5 and 6. For each objective function, the design derivatives are strongest at the root of the wing (where the stresses are expected to be highest), and become much smaller at the tip. This magnitude discrepancy is also noted in the time history of the derivatives seen preceding. Furthermore, there is a chordwise gradient in the sensitivity at the root, though the derivatives are nearly independent of chord position as one travels towards the wing tip. As noted preceding, the derivative of the cycle-averaged lift along the wing is nearly zero.

The C_T design derivatives indicate that the time-averaged thrust force of the plunging wing can be increased by decreasing the thickness at the root, and increasing the thickness at the tip (though the gradients at the tip are very small). Both trends will, presumably, increase the tip deformation, the tip speed, and hence the aerodynamic thrust. The former is an elastic affect, while the latter is an inertial affect (increasing the tip mass). As seen from the lower left corner of Fig. 7, these same changes in the thickness distribution will increase the power as well.

For the efficiency, which is an important metric for propulsive wing design, there is a strong chordwise gradient at the wing root. Efficiency is improved by increasing the thickness at the leading edge, and decreasing the thickness at the trailing edge. It is noted preceding (and experimentally [20]) that the aeroelastic behavior of the plate described in Table 1 is predominantly a bending motion. The chordwise differences seen in the data of Fig. 7 would seem to advocate torsional motions for efficient thrust production. Specifically, a stiff leading edge and a weaker trailing edge should promote adaptive washout along the plate, which has been shown by Zhu [21] to be an efficient aeroelastic response for harmonically-plunging wings.

Finally, a quantitative comparison between the analytical sensitivity analysis and the finite difference study are given in Table 2, for the time-averaged lift, thrust, power, and propulsive efficiency, for the same two finite elements as given in Fig. 5 (x_1) and Fig. 6 (x_{600}). Percentage-difference errors are generally less than 0.1%; lift errors are somewhat higher, though these gradients are very small. It should be noted that the finite difference sensitivities should not be taken as the "true" values, as this technique is known to have many accuracy issues [1]. Regardless, the comparison is very favorable, and the discrepancies may be due to the fact that neither the residual of the aeroelastic subiteration nor the updated Lagrangian loop can be truly driven to zero (Fig. 2), and errors may accumulate over time. Conservation of energy within the integration of both Eqs. (1) and (23) cannot be guaranteed with the generalized-α method [16], as higher modes may unfavorably interact, leading to further errors in the sensitivity analysis.

VI. Optimization Examples

Having favorably assessed the accuracy of the aeroelastic solver and concomitant analytical sensitivity analysis, the framework is now used in a series of gradient-based optimization studies. Three cases are considered: increasing the propulsive forces generated by a

Table 2 Errors in the derivative of the time-averaged lift, thrust, power, and propulsive efficiency with respect to the thickness of two finite elements

	analytical	FD	error		analytical	FD	error
$\partial C_{L,\,ave}/\partial x_1$	-0.0343049	-0.0326745	-4.9898%	$\partial C_{T,\,ave}/\partial x_1$	-1.296253	-1.295923	-0.0255%
$\partial C_{P,\,ave}/\partial x_1$	-5.692078	-5.688146	-0.0691%	$\partial \eta/\partial x_1$	1.154188	1.152888	-0.1127%
$\partial C_{L,\,ave}/\partial x_{600}$	-0.0003526	-0.0003492	-0.0497%	$\partial C_{T,\,ave}/\partial x_{600}$	0.090149	0.090168	-0.0454%
$\partial C_{P,\,ave}/\partial x_{600}$	0.2213107	0.2213518	-0.0669%	$\partial \eta/\partial x_{600}$	-0.009527	-0.009526	-0.0183%

Table 3 Optimization parameters for each case

Case	G^i	I_o	I_f	$x_{\min}$	$x_{\max}$
A	$-C_T$	100	150	0.7 mm	1.3 mm
B	C_P	150	200	0.4 mm	1.6 mm
C	C_L	$i\,(C_L = C_{L,\max})$	$i\,(C_L = C_{L,\max})$	0.4 mm	1.6 mm

harmonically-plunging wing (case A, same as preceding), minimizing the limit cycle amplitude of a fixed wing in a steady freestream (case B), and optimizing the gust alleviation of a fixed wing subject to a vertical gusting velocity (case C). All three problems are very relevant to the current state of aeroelastic design [22], and each is governed by coupled, unsteady, nonlinear, three-dimensional interactions.

For each case, the general optimization problem is formally stated as

$$\min_{\boldsymbol{x}} \; g \quad \text{s.t.:} \begin{cases} x_{\min} < x_n < x_{\max} & n = 1 \ldots N_{\mathrm{DV}} \\ \text{mass} \le \text{mass}_o & \\ \boldsymbol{M}\cdot\ddot{\boldsymbol{u}}^i + \boldsymbol{C}\cdot\dot{\boldsymbol{u}}^i + \boldsymbol{P}^i = \boldsymbol{F}^i & i = 1 \ldots I_f \end{cases} \tag{27}$$

where g, $x_{\min}$, and $x_{\max}$ are problem-dependent objective functions and side constraints (on the thickness of each finite element), as summarized in Table 3. It is further stipulated that the wing mass does not increase over the baseline design during the optimization process, and that the equations of motion [Eq. (1)] are satisfied at each time step. The baseline design is, as preceding, a wing discretized into 600 triangular elements, each with a thickness of 1 mm.

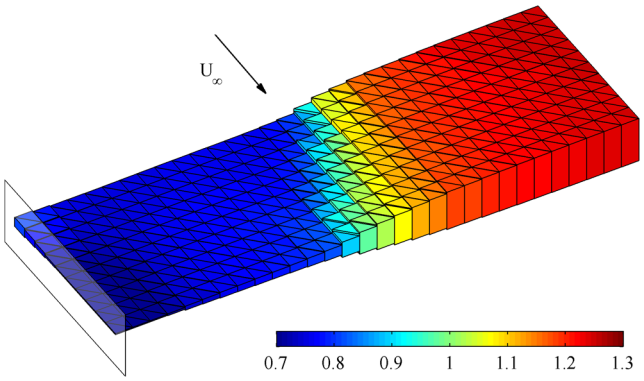

Fig. 8 Thrust-optimal thickness distribution for case A.

A. Plunging Wing Propulsion

For this case, the problem parameters are identical to what is given preceding, and it is desired to maximize the cycle-averaged thrust by tailoring the thickness distribution, without increasing the overall wing mass. This optimal thickness distribution can be seen in Fig. 8, where it should be emphasized that the minimum and maximum shell thicknesses are not to scale with either each other, or the chord/span of the plate. Geometry has been exaggerated to emphasize the thickness variations required for optimal propulsion. The thickness distribution largely parallels the C_T design derivatives seen in Fig. 7: the minimum gage is used near the root (where the stresses will be highest) to increase the overall plate flexibility. Conversely, mass is allocated to the wing tip to increase the inertial forces.

A chordwise variation in mass/stiffness is evident across the plate, presumably to provide a moderate amount of passive wing twist during the plunging motion. As preceding, however, the unsteady deformation is dominated by the first bending mode. Propulsion is optimized (for this case, the mass constraint is not active, i.e., the mass of the design in Fig. 8 is less than the 1 mm uniform plate) by increasing the amplitude of the bending motion, as seen on the right side of Fig. 9, where tip deflection is nearly doubled over the baseline. Care must be taken not to allow the tip motion and the root motion to become too out-of-phase, which has been shown [20] to decrease thrust. As such, the thickest elements at the tip do not reach the design variables' upper bound (1.3 mm, Table 3). The phase lag of the optimal design is still more than the baseline design, but not critically so.

The thrust history given in Fig. 9 is, as preceding, augmented with the experimentally determined C_{Do}, with rigid and baseline data repeated from Figs. 3 and 4. For the time-periodic trends within the third plunging cycle, the improvements in the peak and the cycle-averaged thrust over the baseline design are substantial: from an average C_T of 0.426 to 0.578. Interestingly, the optimal design is also able to tailor its aeroelastic behavior to increase the minimum thrust

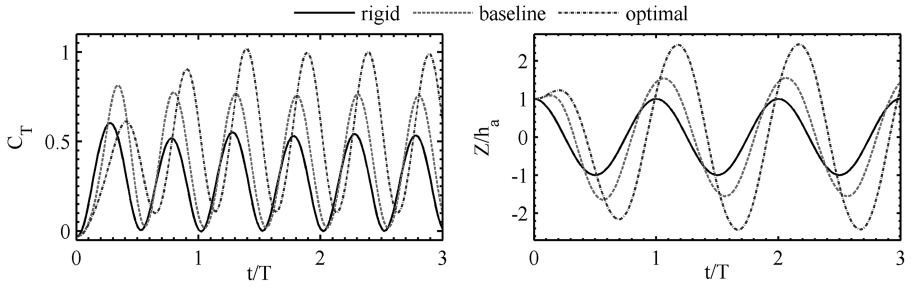

Fig. 9 Propulsion and tip motion for the rigid wing, baseline flexible wing, and optimal flexible wing.

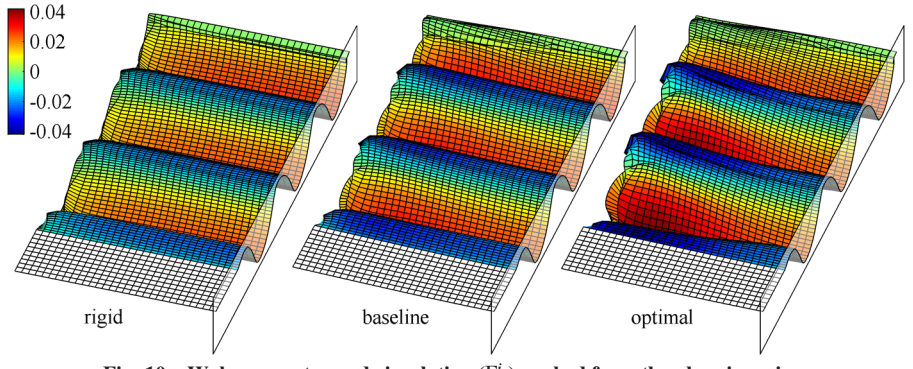

Fig. 10 Wake geometry and circulation (Γ_w^i) as shed from the plunging wing.

Table 4 Aeroelastic parameters for case B

Property	Value	Property	Value
Chord, c	0.1 m	Elastic modulus, E	210 GPa
Semispan, $b/2$	0.3 m	Poisson's ratio, ν	0.3
Flow velocity, U_∞	120 m/s	Plate density, ρ_{wing}	7800 kg/m^3
Flow density, ρ_{fluid}	1.225 kg/m^3	Angle of attack, α	0.1°

Table 5 Aeroelastic parameters for case C

Property	Value	Property	Value
Chord, c	0.1 m	Elastic modulus, E	210 GPa
Semispan, $b/2$	0.3 m	Poisson's ratio, ν	0.3
Flow velocity, U_∞	40 m/s	Plate density, ρ_{wing}	7800 kg/m^3
Flow density, ρ_{fluid}	1.225 kg/m^3	Gust speed, W_{gust}	8 m/s
Angle of attack, α	0°	Gust frequency, ω_{gust}	100, 20 rad/s

during the motion, much more effectively than the baseline design (whose minimum is roughly the same as the rigid wing). This is due to the aforementioned phase lag; at each point in the cycle, some location along the plate, either the root or the tip, has enough vertical velocity to produce thrust.

The optimal design is very successful in the final plunging cycle (as designed, Table 3), but the initial thrust is much lower than the baseline design's. This would indicate that an aeroelastic design for rapid, agile acceleration and maneuvering may be very different than the design for steady, continuous propulsion seen in Fig. 8. The baseline flexible design may provide the better compromise between the two flight modes.

Finally, the wake structures shed from the rigid, baseline flexible, and optimal flexible wings are given in Fig. 10, where the contour strengths are Γ_w^i, from Eq. (4). Only the newest ten rows of wake rings shed off the trailing edge are freely deformed to follow the streamlines within the wake, with the remainder held fixed where they lay. This has been shown to reduce the computational cost considerably, with no significant effect upon the accuracy [23]. Stronger pockets of high circulation are seen in the wake aft of the optimal design, as well as larger tip vortex swirling and wake deformation at the tip, all indicative of the larger aerodynamic forces. The wake strength and shape directly aft of the root is very similar for each wing, however, as the plate is fully clamped here, and the sinusoidal motion is prescribed.

B. Limit Cycle Oscillations

When a flexible wing operates at a flight speed above its Hopf-bifurcation point (i.e., flutter speed), the aeroelastic damping becomes negative, the wing extracts energy from the flow, and the vibratory motion becomes unbounded [12]. The presence of a nonlinearity may arrest this instability, however, leading to the formation of a limit cycle oscillation [24]. Three such nonlinearities are present in the aeroelastic model discussed in Sec. II. The deformation of the wake rings along local streamlines is a mild nonlinearity [18], wing motion $\boldsymbol{z}^i$ alters the influence matrix $\boldsymbol{C}_1^i$ in a very nonlinear manner (as dictated by the Biot–Savart law), and of course large geometric nonlinearities are included in the shell model [Eq. (2)]. The latter effect is thought to be the principle cause of the limit cycle oscillation (LCO) formations studied here.

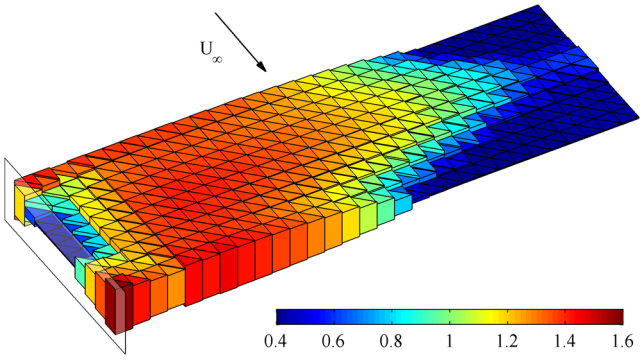

Fig. 11 LCO-optimal thickness distribution for case B.

For this case, the shape and structure of the baseline rectangular wing are the same as preceding, but the shell is fixed at a small angle of attack, with no overall rigid body plunging motion. Furthermore, the surrounding fluid is now air, as summarized in Table 4. The flutter point of the baseline wing (as preceding, a uniform thickness of 1 mm) is estimated to be 92 m/s (as computed with a linear direct flutter solver described in [25]: see verification and validations studies presented therein). The operating speed is 120 m/s, and so a limit cycle is expected. It is desired to minimize the amplitude of the LCO without, as preceding, increasing the overall wing mass. While it is possible to reformulate the aeroelastic equations of motion such that the amplitude is explicitly handled [26], for this work, minimizing the average pressure coefficient over the last several cycles (once the LCO has fully developed) was found to be an adequate surrogate within the framework described preceding.

The resulting optimal thickness distribution is given in Fig. 11. For this case, unlike case A, the mass constraint [Eq. (27)] is active: the optimal design and the baseline design have the same mass. Presumably, removing this constraint would provide a design with superior stability requirements to the one discussed here. The optimal design increases the thickness of the leading and trailing edge at the root, while the center of the root and the material at the wing tip approach the lower bound on thickness. A time history of the deflection at the tip can be found in Fig. 12, normalized by the baseline thickness of the plate (1 mm). The angle of attack (0.1°) provides a perturbation to the aeroelastic system, and the resulting LCO has a mean value offset from the trivial solution.

For the baseline design, as the operating flight speed is well above the flutter speed, the LCO amplitude is very large and sets up quickly. The out-of-plane tip displacement ranges from −15 to 22 baseline thicknesses (1 mm), and the in-plane foreshortening (whose LCO has twice the frequency as the out-of-plane motion, and whose existence is the hallmark of a nonlinear aeroelastic plate [24]) is roughly one thickness in amplitude. Conventional tools for nonlinear aeroelasticity typically incorporate von Kármán models of lower-fidelity [26]. The ability of these models to handle such large deflections in an accurate manner is doubtful however: the corotational updated

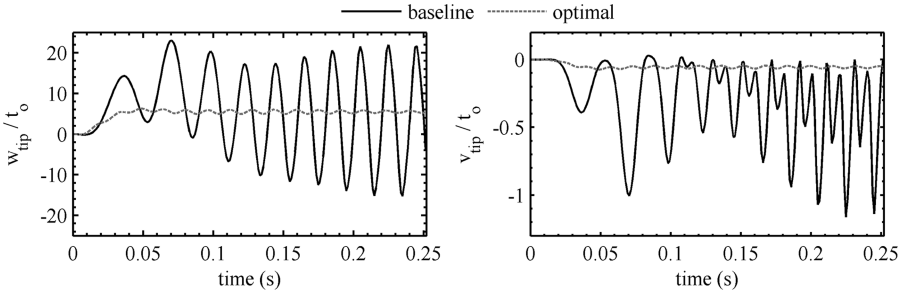

Fig. 12 Out-of-plane (left) and in-plane (right) tip deflection LCO development.

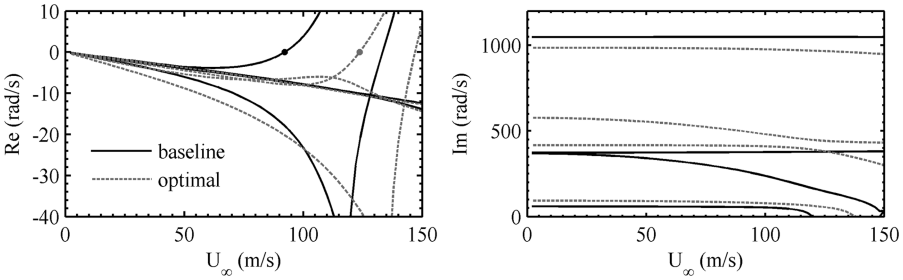

Fig. 13 Real (left) and imaginary (right) eigenvalues of the linearized aeroelastic system.

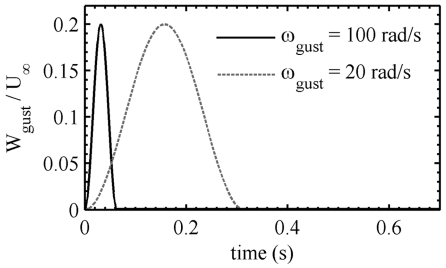

Fig. 14 Gust velocity time histories.

Largrangian shell description used preceding (or a similar level of fidelity) may be required.

The redistribution of mass and stiffness seen in Fig. 11 has increased the flutter speed to 123.5 m/s. The real and imaginary portions of the lowest four eigenvalues of the linearized aeroelastic system (as preceding, computed with the linear direct flutter solver described in [25]) are given in Fig. 13 for both the baseline and optimal wing structures as a function of flight speed. The upwards shift in flutter speed due to the aerostructural optimization is clearly seen. The thickness distribution of Fig. 11 has drastically altered the nature of the flutter mechanism; for the baseline design, a loss of aeroelastic stability corresponds to a moderate coalescence of the first two modes (bending and twisting). For the optimal design, the higher flutter speed is a stronger coalescence of the second and third modes. The shift in the linear flutter speed is a natural by-product of the optimal design, which is successfully designed to attenuate the limit cycle seen in Fig. 12. As the new flutter speed is slightly above the operating speed of 120 m/s, the system is stable, and the oscillations about the static perturbation gradually decay to a static aeroelastic solution at an angle of attack of 0.1° for both in-plane and out-of-plane motion. The rate of decay is very slow, however, as the damping will be small (but stable) just below the flutter point.

C. Gust Alleviation

The final case study considered here is that of prudent thickness and mass redistribution along a flexible wing for passive alleviation of a gust. The aeroelastic parameters are summarized in Table 5. The baseline wing shape and structure is identical to the previous two cases, the flight speed of the air has been decreased to 40 m/s, and the angle of attack is zero. A vertical gust velocity is considered along the Z-axis of Fig. 1, with a $1 - \cos$ time history, as plotted in Fig. 14. The peak velocity of the gust is 20% of the forward flight speed (U_∞), and two gust frequencies are considered: 100 and 20 rad/s. After the first time period (T_{gust}), the vertical flow is removed, and the wing

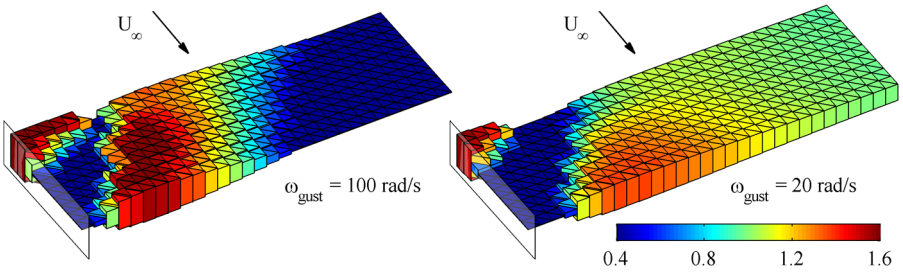

Fig. 15 Gust-optimal thickness distributions for case C.

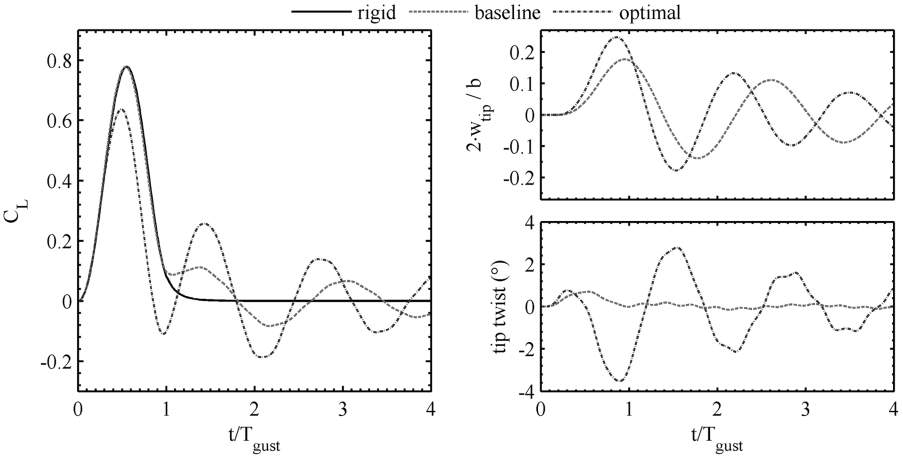

Fig. 16 Aeroelastic time history due to a gust frequency of 100 rad/s.

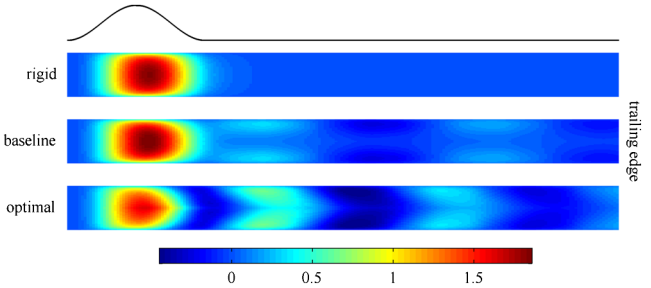

Fig. 17 Wake circulation shed during and after the gust, $\omega_{gust} = 100$ rad/s.

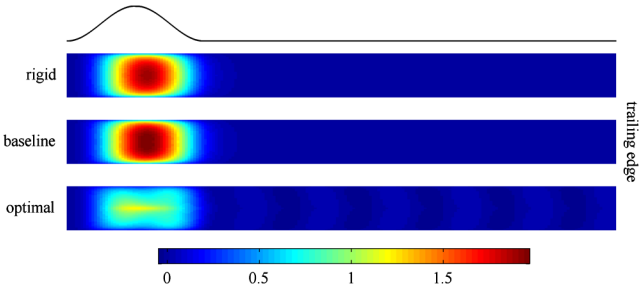

Fig. 19 Wake circulation shed during and after the gust, $\omega_{gust} = 20$ rad/s.

vibrates under the influence of the forward flow alone. As the angle of attack is now zero, stable oscillations should eventually decay to the trivial aeroelastic solution (zero shell displacement, zero aerodynamic pressure). It should be noted that, though two different gust frequencies are considered (and do not result in drastically different structural designs, as discussed next), a worst-case gust via matched filter theory [27] is not considered here.

The optimal thickness distributions for both gust frequencies are seen in Fig. 15. Like case A, the mass constraint is inactive for both frequencies. The two designs share many similarities, with the thickness of the leading edge at the root brought to the upper bound, and the remainder of the root to the lower bound. Thicknesses at the wing tip differ substantially, however, with the low-frequency case much heavier and stiffer in this region. Focusing first on the higher frequency, Fig. 16 gives the time history of the rigid, flexible baseline, and flexible optimal designs. The reduced gust frequency is low ($k_{gust} = \omega_{gust} \cdot c/2/U_\infty = 0.125$): unsteady aerodynamic effects are moderate, and the lift coefficient of the rigid wing closely follows the gust profile. The influence of the wake upon the aerodynamic forces is similarly muted, and the lift of the rigid wing quickly becomes zero after the first gust period. Similar trends are also seen in the wake strength (Γ_w^i) of Fig. 17, where large circulations are indicative of high wing lift. Shortly after the gust, the circulation shed from the trailing edge is nearly zero.

From a structural standpoint, however, unsteady effects are very pronounced, as the first natural bending frequency of the baseline wing is 59.2 rad/s (noted in Fig. 13), well below the gust frequency. The time lag between the response and the loading is large, as the gust occurs very rapidly. The wing bending is still zero at $t/T_{gust} = 0.5$, and reaches a peak value (of 17% of the wing length or semispan, providing moderate geometric nonlinearities) as the gust concludes. The lift coefficient during the gust is nearly identical to the rigid wing, but oscillations about zero lift are seen for the remainder of the simulation, and in the wake history as well (Fig. 17), where aerodynamic forces are generated by the bending motion of the wing. The operating speed for this case is below the flutter speed, and the vibrations decay in a stable manner.

Because the response time of the structure is so slow, passive gust alleviation for this case is only moderately successful. The design is arrived at by minimizing the peak lift seen during the gust (Table 3), and the resulting thickness distribution (Fig. 15, left) imparts a degree of negative bend-twist coupling, where a positive deflection of the tip causes the wing to washout, alleviating the flight loads. This strategy towards load rejection is sound [28] but as noted, the gust occurs too quickly. An increased tip deflection of the optimal design is accompanied by a negative tip twist (Fig. 16), which decreases the peak lift and the peak circulation shed from the trailing edge (Fig. 17) by 15%. An unintended consequence of the optimization is that the wing deformation, aerodynamic forces, and wake strength during the time periods after the gust, though dynamically stable, are much larger than for the baseline case. Reformulating the optimization problem in order to minimize the power coefficient over the entire simulation (both during and after the gust) may be able to strike a better compromise between gust alleviation and postgust response, but was not considered here.

Similar results are given in Figs. 18 and 19 for a gust frequency of 20 rad/s. This frequency is now a third of the wing's resonance frequency, providing more time for the passive deformation to react to the change in flight loads. For the uniform baseline wing, a positive bend-twist coupling causes the bending wing to slightly wash-in, increasing the peak lift (and the peak wake circulation) as compared with the rigid wing. In contrast to the previous gust frequency, very little postgust aeroelastic response is observed. A negative bend-twist coupling is built into the optimal design as before (Fig. 15), which is able to drop the peak lift and the peak wake disturbance by half. Most of this alleviation is due to the washout, but some is also due to the large bending velocities of the wing, which counteract the gust by bringing the total velocity of the vortex rings near the wing tip closer to zero.

It can be seen that the gradient-based optimization has substantially lowered the peak lift coefficient as intended, but the design is now operating close to its flutter speed. Postgust deformation, flight loads, and wake strength, though stable, decay very slowly (as the aerodynamic damping at the Hopf-bifurcation is zero

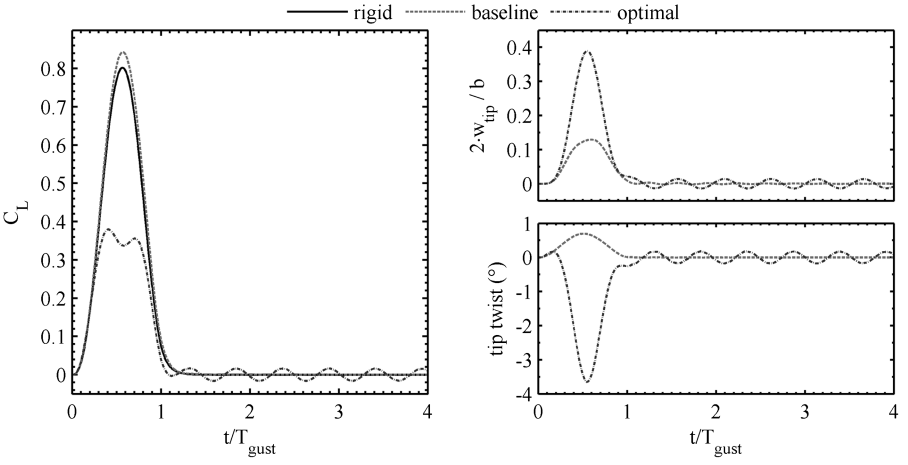

Fig. 18 Aeroelastic time history due to a gust frequency of 20 rad/s.

[24]). This is presumably due to the fact that adaptive washout, though beneficial for static divergence and gust alleviation, has the opposite effect on the flutter margin, a phenomenon which prefers wash-in [27]. As before, a global-time power minimization may be able to prevent this development during the optimization, or potentially an objective function with normalized contributions from the gust response and the postgust response.

VII. Conclusions

This work has detailed the analytical sensitivity analysis of a numerical framework aimed at computing nonlinear, unsteady, three-dimensional aeroelastic response. Specifically, a nonlinear shell model (a corotational approximation of the updated Lagrangian approach) is coupled to an unsteady vortex lattice method with a time evolving wake structure. This system response is computed with an implicit time marching scheme, with two nested loops within each time step to accommodate various coupled nonlinearities. The model is validated against experimental data for a plunging wing in a water tunnel.

It is desired to compute the analytical derivative of an aerodynamic force quantity with respect to a large vector of structural design variables, a vector whose cross-disciplinary nature emphasizes the coupled nature of the problem. This is done with a direct approach, formulating a second differential equation for the design gradients which is linear, with time-varying coefficients and multiple right-hand-sides (one per design variable). This equation can be solved in conjunction with the nonlinear differential equation governing the system response, as opposed to the adjoint method, which provides a differential equation which must be integrated in reverse (albeit one that is independent of the nature of the design variable vector). For the problem considered here, the adjoint method should be more expensive, computationally [6]. These derivatives are favorably verified with a costly finite difference analysis.

Finally, the gradients are used for aeroelastic optimization of three distinct design problems: propulsive force development of a harmonically-plunging wing, limit cycle oscillations of a fixed wing, and gust alleviation. All three cases are governed by coupled, unsteady, nonlinear aeroelasticity, and thus provide suitable cases for the current research effort. The analytically-computed gradients provided to the optimizer are able to tailor the stiffness and mass distributions throughout the wing to produce the desired effect for all three, though unintended consequences are observed for the latter (and most challenging) gust alleviation case study.

Acknowledgments

This work is sponsored by the Air Force Office of Scientific Research under Laboratory Task 03VA01COR (monitored by Fariba Fahroo). The research was performed while the first author held a National Research Council Associateship Award at AFRL.

References

[1] Haftka, R., and Gürdal, Z., *Elements of Structural Optimization*, Kluwer, Dordrecht, The Netherlands, 1992.

[2] Le Moigne, A., and Qin, N., "Variable-Fidelity Aerodynamic Optimization for Turbulent Flows Using a Discrete Adjoint Formulation," *AIAA Journal*, Vol. 42, No. 7, 2004, pp. 1281–1292. doi:10.2514/1.2109

[3] Kim, N., and Choi, K., "Design Sensitivity Analysis and Optimization of Nonlinear Transient Dynamics," AIAA Symposium on Multi-disciplinary Analysis and Optimization, Long Beach, CA, AIAA Paper 2000-4905, 6–8 Sept. 2000.

[4] Trier, S., Marthinsen, A., and Sivertsen, O., "Design Sensitivities by the Adjoint Variable Method in Nonlinear Structural Dynamics," SIMS Simulation Conference, Norwegian Inst. of Science and Technology, Trondheim, Norway, June 1996.

[5] Beran, P., Stanford, B., and Kurdi, M., "Sensitivity Analysis and Optimization of Dynamic Systems with Reduced Order Modeling," AIAA Aerospace Sciences Meeting, Orlando, FL, AIAA Paper 2010-1503, 4–7 Jan. 2010.

[6] Martins, J., Alonso, J., and Reuther, J., "A Coupled-Adjoint Sensitivity Analysis Method for High-Fidelity Aero-Structural Design," *Optimization and Engineering*, Vol. 6, No. 1, 2005, pp. 33–62. doi:10.1023/B:OPTE.0000048536.47956.62

[7] Stanford, B., and Ifju, P., "Aeroelastic Topology Optimization of Membrane Structures for Micro Air Vehicles," *Structural and Multidisciplinary Optimization*, Vol. 38, No. 3, 2009, pp. 301–316. doi:10.1007/s00158-008-0292-x

[8] Giunta, A., "A Novel Sensitivity Analysis Method for High Fidelity Multidisciplinary Optimization of Aero-Structural Systems," AIAA Aerospace Sciences Meeting, Reno, NV, AIAA Paper 2000-683, 10–13 Jan. 2000.

[9] Maute, K., Nikbay, M., and Farhat, C., "Sensitivity Analysis and Design Optimization of Three-Dimensional Non-Linear Aeroelastic Systems by the Adjoint Method," *International Journal for Numerical Methods in Engineering*, Vol. 56, No. 6, 2003, pp. 911–933. doi:10.1002/nme.599

[10] Barcelos, M., and Maute, K., "Aeroelastic Design Optimization for Laminar and Turbulent Flows," *Computer Methods in Applied Mechanics and Engineering*, Vol. 197, No. 19, 2008, pp. 1813–1832. doi:10.1016/j.cma.2007.03.009

[11] Seyranian, A., "Sensitivity Analysis and Optimization of Aeroelastic Stability," *International Journal of Solids and Structures*, Vol. 18, No. 9, 1982, pp. 791–807. doi:10.1016/0020-7683(82)90036-1

[12] Odaka, Y., and Furuya, H., "Robust Structural Optimization of Plate Wing Corresponding to Bifurcation in Higher Mode Flutter," *Structural and Multidisciplinary Optimization*, Vol. 30, No. 6, 2005, pp. 437–446.

[13] Mani, K., and Mavriplis, D., "Adjoint-Based Sensitivity Formulation for Fully Coupled Unsteady Aeroelasticity Problems," *AIAA Journal*, Vol. 47, No. 8, 2009, pp. 1902–1915. doi:10.2514/1.40582

[14] Madenci, E., and Barut, A., "Dynamic Response of Thin Composite Shells Experiencing Nonlinear Elastic Deformations Coupled with Large and Rapid Overall Motions," *International Journal for Numerical Methods in Engineering*, Vol. 39, No. 16, 1996, pp. 2695–2723. doi:10.1002/(SICI)1097-0207(19960830)39:16<2695::AID-NME955>3.0.CO;2-1

[15] Cook, R., Malkus, D., Plesha, M., and Witt, R., *Concepts and Applications of Finite Element Analysis*, Wiley, New York, 2002.

[16] Kuhl, D., and Crisfield, M., "Energy-Conserving and Decaying Algorithms in Non-Linear Structural Dynamics," *International Journal for Numerical Methods in Engineering*, Vol. 45, No. 5, 1999, pp. 569–599. doi:10.1002/(SICI)1097-0207(19990620)45:5<569::AID-NME595>3.0.CO;2-A

[17] Stanford, B., and Beran, P., "Cost Reduction Techniques for the Structural Design of Nonlinear Flapping Wings," AIAA Structures, Structural Dynamics, and Materials Conference, Palm Springs, CA, AIAA Paper 2009-2414, 4–7 May 2009.

[18] Katz, J., and Plotkin, A., *Low-Speed Aerodynamics*, Cambridge Univ. Press, Cambridge, England, U.K., 2001.

[19] Stanford, B., and Beran, P., "Analytical Sensitivity Analysis of an Unsteady Vortex Lattice Method for Flapping Wing Optimization," *Journal of Aircraft*, Vol. 47, No. 2, 2010, pp. 647–662. doi:10.2514/1.46259.

[20] Heathcote, S., Wang, Z., and Gursul, I., "Effect of Spanwise Flexibility on Flapping Wing Propulsion," *Journal of Fluids and Structures*, Vol. 24, No. 2, 2008, pp. 183–199. doi:10.1016/j.jfluidstructs.2007.08.003

[21] Zhu, Q., "Numerical Simulation of a Flapping Foil with Chordwise or Spanwise Flexibility," *AIAA Journal*, Vol. 45, No. 10, 2007, pp. 2448–2457. doi:10.2514/1.28565

[22] Livne, E., "Future of Airplane Aeroelasticity," *Journal of Aircraft*, Vol. 40, No. 6, 2003, pp. 1066–1092. doi:10.2514/2.7218

[23] Fritz, T., and Long, L., "Object-Oriented Unsteady Vortex Lattice Method for Flapping Flight," *Journal of Aircraft*, Vol. 41, No. 6, 2004, pp. 1275–1290. doi:10.2514/1.7357

[24] Tang, D., Dowell, E., and Hall, K., "Limit Cycle Oscillations of a Cantilevered Wing in Low Subsonic Flow," *AIAA Journal*, Vol. 37, No. 3, 1999, pp. 364–371. doi:10.2514/2.717

[25] Stanford, B., and Beran, P., "Optimal Structural Topology of a Plate-Like Wing for Subsonic Aeroelastic Stability," AIAA Structures, Structural Dynamics, and Materials Conference, Orlando, FL, AIAA Paper 2010-2841, 12–15 April 2010.

[26] Beran, P., and Lucia, D., "A Reduced Order Cyclic Method for Computation of Limit Cycles," *Nonlinear Dynamics*, Vol. 39, No. 1, 2005, pp. 143–158.
doi:10.1007/s11071-005-1921-1

[27] Kanda, A., and Dowell, E., "Worst-Case Gust-Response Analysis for Typical Airfoil Section with Control Surface," *Journal of Aircraft*, Vol. 42, No. 4, 2005, pp. 956–962.
doi:10.2514/1.8931

[28] Shirk, M., Hertz, T., and Weisshaar, T., "Aeroelastic Tailoring: Theory, Practice, and Promise," *Journal of Aircraft*, Vol. 23, No. 1, 1986, pp. 6–18.
doi:10.2514/3.45260

E. Livne
Associate Editor